

LOW-SPEED EXPERIMENTAL INVESTIGATION OF PODDED ENGINE INTEGRATION OF FLYING V AIRCRAFT

Ankit Kumar[1] & Roelof Vos[2]

[1 2]Faculty of Aerospace Engineering, Delft University of Technology, Kluyverweg 1, 2629 HS Delft

Abstract

Engine integration remains a key challenge in realizing the aerodynamic and fuel-efficiency benefits of flying-wing transport aircraft such as the Flying V. This study experimentally investigates the aerodynamic performance of a 4.6% scale Flying V wind tunnel model with a powered nacelle at a freestream velocity of 25 m/s. The mass flow ratio (MFR) was varied to simulate windmilling, cruise, and takeoff conditions at MFR = 0.3, 0.7, and 2.1, respectively. Aerodynamic forces, inlet pressure recovery, and nacelle inlet distortion were evaluated across these conditions. The engine-installed configuration produced the highest lift coefficient at MFR = 2.1 at an angle of attack of $\alpha = 14°$, approximately 13% higher than the isolated wing. The net vehicle force coefficient was minimal at MFR = 2.1, with thrust being ten times higher than drag at $\alpha = 0°$ and thrust being equal to drag at $\alpha = 20°$. Inlet pressure recovery remained above 95% up to $\alpha = 6°$ and $\alpha = 4°$ for MFR = 0.3 and 0.7, respectively. For MFR = 2.1, pressure recovery remained above 85% up to $\alpha = 4°$. Minimum local pressure recovery decreased with increasing MFR and shifted from the lower AIP region to the upper outboard wing region with increasing angle of attack. Distortion metrics (DC_{60} and DC_{180}) showed maximum distortion at MFR = 2.1, reaching approximately 43% at $\alpha = 8°$ and 25% at $\alpha = 18°$, respectively, consistent with regions of lowest local pressure recovery.

Keywords: nacelle inlet testing, mass flow ratio, pressure recovery

1. Introduction

Since the first powered flight in 1903, aviation has advanced rapidly through improvements in propulsion, aerodynamics, and avionics, making air transportation faster, safer, and more affordable. The tube-and-wing (TAW) configuration has dominated commercial aviation for more than 100 years. Despite these advancements, aviation's contribution to energy-related emissions, approximately 2% [1], necessitates urgent action. Emerging concepts, such as the FLYING V™[1] aircraft, a flying wing configuration, pursue further fuel efficiency gains (Figure 1). This innovative design aims to significantly improve efficiency, reducing fuel burn by 20% at cruise compared to conventional aircraft like the A350-1000. The Flying V features an over-the-wing engine configuration and integrates the passenger cabin, cargo hold, and fuel tanks within the wing structure, offering a promising step toward more sustainable aviation.

The concept was conceived by German engineer Dr. Justus Benad during his 2015 internship at Airbus Hamburg [2]. Researchers at the Faculty of Aerospace Engineering at TU Delft subsequently investigated the design through wind-tunnel experiments [3, 4], flying-scale model tests [5], and simulations in the SIMONA flight simulator [6, 7, 8]. By the early 2020s, the team had grown to over 20 researchers working on aircraft design [9], flight control [10], and climate impact [11, 12]. Benad later joined the project as a postdoctoral researcher and chief engineer, amongst others, overseeing the aerodynamic design optimization [13].

[1]Flying V is a trademark of Fortescue. The Flying V design is owned by Fortescue, UK & NL patents pending.

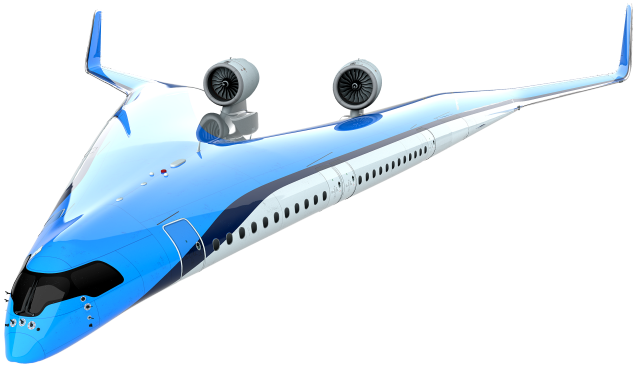


Figure 1 – Artist impression of the Flying V aircraft

Research has been conducted on integrating engines with the Flying V aircraft. A study by Rubio-Pascual and Vos explored aerodynamic performance during engine integration by analyzing the lift-to-drag (L/D) ratio for various engine placements [14]. Using Euler-based computational fluid dynamics (CFD), the research recommended an engine location that minimized the penalty to the lift-to-drag ratio: $X/L = 0.68$, $2Y/b = 0.18$, and $Z/\overline{c} = 0.05$ in the aircraft reference frame. The research highlighted that misplacing the engine could detrimentally impact the Lift-to-Drag ratio up to 55% and estimated an aerodynamic penalty of 10% upon integration at the proposed location. In addition, reducing the spacing between the nacelles of the two engines created a convergent-divergent channel that generated strong shockwaves.

Another study by Van Empelen and Vos experimentally investigated a 4.6%-scaled wind tunnel at low-speed conditions [15]. The engine was located at $X/L = 0.60$, $2Y/b = 0.16$, and $Z/\overline{c} = 0.11$, and the experiment was conducted in the open jet facility (OJF) of TU Delft. At angles of attack more than 5°, interference drag was observed, with a maximum increase of 16.5% at $\alpha = 10^\circ$, while at lower angles, engine operation reduced airframe drag. The highest interference drag penalty of 60 counts was at 10° angle-of-attack. The interference effects on the lift and pitching moment were of the same order of magnitude as the installation effects due to thrust. This indicates that the thrust of the engine and its interaction with the wing must be considered in aerodynamic analysis.

Another study by Kumar and Vos computationally simulated the full-scale Flying V aircraft [16] at cruise and take-off operating conditions with $Re_{\overline{c}} = 100$ million. The results showed that the configuration achieves high aerodynamic efficiency, as indicated by the lift-to-drag ratio, consistent with the improved aerodynamic design of Laar et al. [13], who conducted RANS simulations at cruise and implemented design changes to increase the lift-to-drag ratio. Furthermore, the results from Kumar and Vos in [16] demonstrated that the configuration can achieve high aerodynamic efficiency while enabling feasible over-wing engine integration when engines are positioned within specific low-distortion flow regions identified through CFD analysis. The study further concluded that although acceptable inlet distortion levels are achievable, additional flow-control strategies or design optimization may be required to ensure robust engine performance across off-design flight conditions.

Both studies from Ref. [14] and Ref. [15] indicate a strong mutual interaction between the wing flow and the nacelle. Since the engine is located near the trailing edge of the wing, the nacelle intake flow is strongly influenced by the wing wake, thereby directly affecting inlet pressure recovery. As a result, the pressure distribution both inside the inlet and over the nacelle differs from that of a conventional under-the-wing engine configuration. The present research aims to investigate the effects of engine installation on overall aerodynamic performance and nacelle inlet characteristics.

This paper is structured as follows. In Section 2. the experimental setup is presented along with the design of the nacelle test article. In Section 3., the results are presented. We show how a variation in angle of attack and mass flow ratio influences the force coefficients, the inlet pressure recovery and

the distortion. Conclusions are drawn in Section 4..

2. Methodology

The following section describes the experimental configuration, measurement instrumentation, operating conditions, as well as the data acquisition and processing procedures. The experiments are conducted in the Open Jet Facility (OJF) at TU Delft.

2.1 Experimental Setup

Figure 2 shows the scaled Flying V wind-tunnel model with the nacelle installed in the Open Jet Facility. The model is half-wing with a 1500 mm span and 820 mm mean aerodynamic chord $(\bar{c})$ [17]. As can be seen, the nacelle is supported by a strut and is not connected to the Flying V wing.

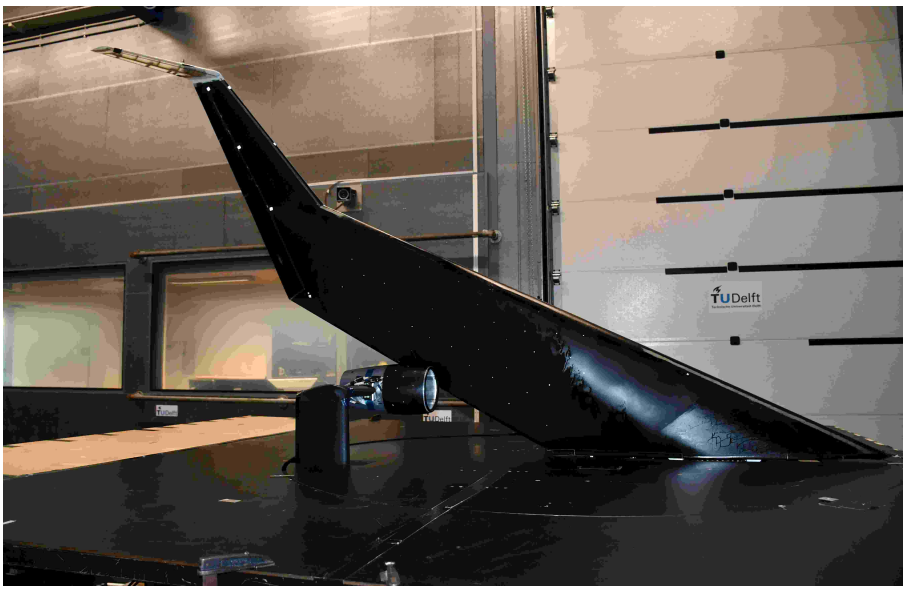
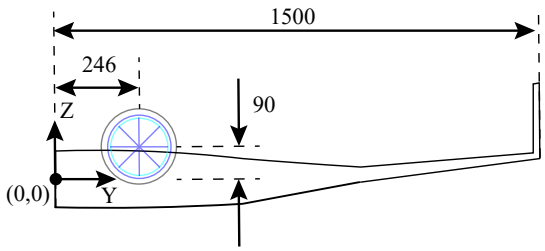
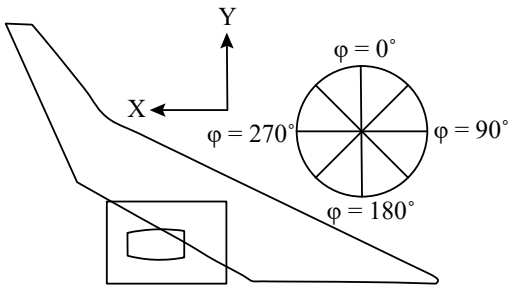


Figure 2 – Wind-tunnel setup of a 4.6% scaled Flying V wing and a strut-mounted nacelle equipped with an electric motor and fan.

The nacelle design, derived from the NASA Common Research Model (CRM) [18], is made axisymmetric by revolving a single CRM section about its longitudinal axis. The original CRM nacelle profile is retained up to $0.45L_{\text{nac}}$, beyond which the aft section is extended to accommodate the ducted fan required to achieve the desired mass flow ratios. To replicate the propulsion effects, a nacelle equipped with an electrically-powered ducted fan is mounted on the model, as shown in Fig. 4. The fan is operated at two mass flow ratios (MFR), 0.7 and 2.1, by adjusting the throttle settings. A perforated plate is installed in the nacelle exhaust to reduce the mass flow and achieve a mass-flow ratio of 0.3.



(a) Front view showing the spanwise and vertical dimensions.



(b) Top view showing the nacelle location and the azimuthal positions of the total-pressure rakes, annotated by the azimuth angle, φ.

Figure 3 – Schematic of the 4.6%-scale test article including dimensions in millimeters.

Figure 3 presents a schematic drawing of the test article. Figure 3a shows the front view of the over-the-wing nacelle installation and its location in the vertical (Z) and spanwise (Y) directions for the half-wing test article. Figure 3b shows a top view of the test article along with a front view of the aerodynamic interface plane (AIP) showing the definition of the azimuth angle, φ.

2.2 Force Measurements

A six-component strain-gauge balance is mounted on a turntable secured to the support table, with aerodynamic loads from the wing and engine transmitted through a stiff aluminium beam. The splitting plane is aligned with the nozzle exit to shield the balance from downstream flow effects, while the reflection plane was positioned in clean flow to ensure an undisturbed boundary layer. Aerodynamic forces were measured at various angles of attack and mass flow ratios (MFRs). A dedicated force-accounting framework is given below to enable consistent interpretation of the installed aerodynamic forces. Using the bookkeeping symbols defined in Ref. [15], each component in the experimental setup has its own designation as shown in Table 1.

Table 1 – Bookkeeping Nomenclature

W	Wing
N	Nacelle
S	Engine Strut
E	Engine thrust
P	Propulsion system

$$\mathrm{P}=\mathrm{N}+\mathrm{E} \tag{1}$$

where P denotes the total propulsion system contribution, N denotes the unpowered nacelle contribution, and E denotes the powered engine thrust contribution. In the present work, only the isolated wing configuration W and the fully installed powered configuration WSP are available. The implications of this reduced configuration availability for the interpretation of measured force coefficients are discussed below.

$$\mathrm{WSP}=\mathrm{W}+\mathrm{SP} \tag{2}$$

The measurements presented in Section 3. correspond to two primary configurations: the isolated wing configuration (W) and the fully installed powered configuration (WSP). The WSP configuration represents the wing with the nacelle and ducted fan installed and the engine operating, whereas W represents the isolated wing without propulsion integration. The mass flow ratio (MFR) of 0.3 requires a slightly different interpretation. For MFR = 0.3, the ducted fan was switched off and replaced with a perforated plate, as discussed in Section 2.1, to simulate a reduced mass flow condition.

All force coefficients are reported in the wind-axis coordinate system. The net vehicle lift coefficient $\tilde{C}_L$ and net vehicle axial-force coefficient $\tilde{C}_X$ are reported for both the isolated wing (W) and the wing–nacelle–ducted fan configuration (WSP). These coefficients represent the total vehicle forces acting in the lift and axial directions, respectively. In the axial direction, the force includes both aerodynamic drag and propulsive thrust contributions. Therefore, more negative values of $\tilde{C}_X$ correspond to higher net propulsive thrust.

Because only the isolated wing and fully installed powered configurations are available, the reported force coefficients represent the combined effects of nacelle installation, aerodynamic interference, and powered propulsion effects, and cannot be decomposed into individual aerodynamic and propulsion contributions.

2.3 Pressure Measurements

On the aerodynamic interface plane (AIP), eight rakes with total and static pressure probes are installed. Figure 4 illustrates the nacelle and inlet geometry, including the locations of the surface static-pressure taps. Pressure taps are installed on the inside and outside of the inlet up to $0.45\,L_{\mathrm{nac}}$. The AIP diameter is scaled from the full-scale dimensions reported in Ref. [16]. A schematic of the

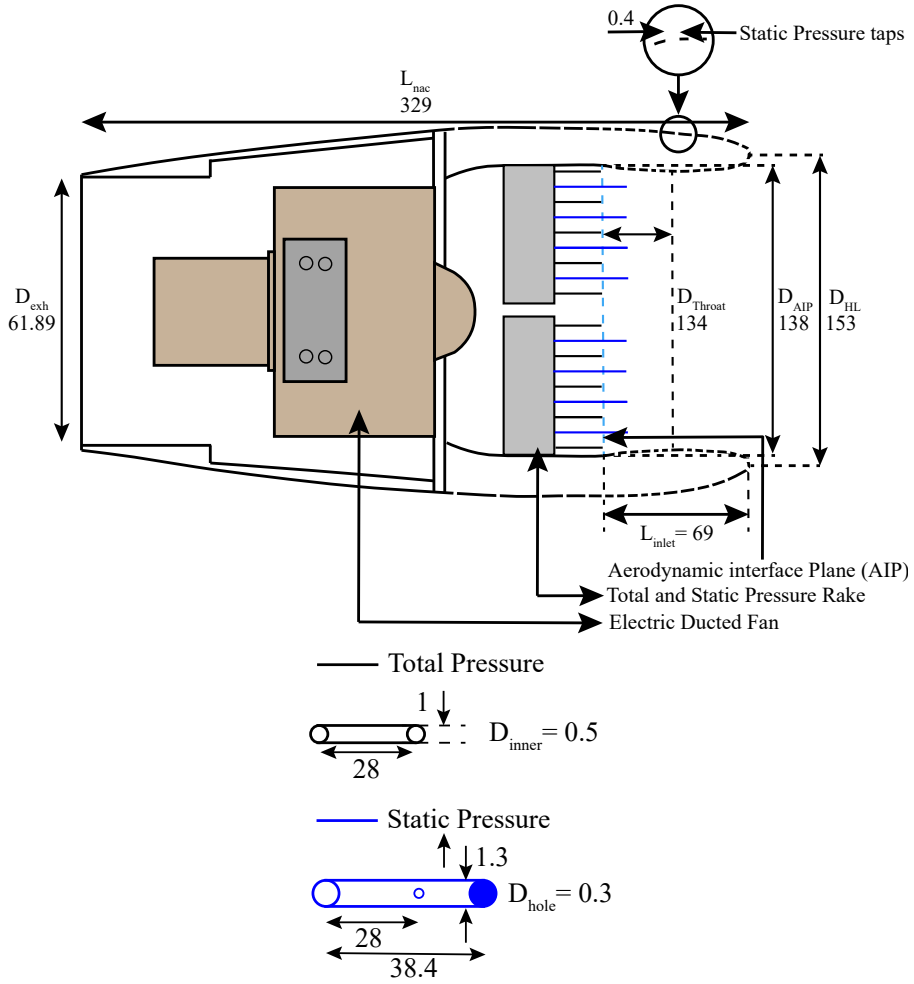


Figure 4 – Schematic of the nacelle cross-section showing surface static-pressure taps, a rake for static and total-pressure measurements at the Aerodynamic Interface Plane (AIP), and the electric ducted fan. All dimensions are given in millimetres (mm). *Not to scale*

rake configuration is shown in Figure 5, illustrating the nacelle diameters at various axial locations and the azimuthal positions of the probes at the AIP. The AIP rake measures total pressure at 40 uniformly distributed locations. The setup employs eight rakes, each equipped with five radial probes, to capture inlet distortion patterns. In addition, 32 static-pressure ports are installed on the Aerodynamic Interface Plane (AIP) to resolve velocity variations across the plane through area averaging. The static pressure probes are designed following the recommendations of Ref. [19] and are implemented to minimize local acceleration effects near the probe tip. Multiple pressure scanners are employed in this setup, including two NUB scanners and a Surrey Sensors DPS14-1K0 unit. Each measurement is conducted for 10 s, with sampling frequencies of 1 kHz for the Surrey Sensors unit and 2 kHz for the NUB scanners. The pressure uncertainty consisted of a Type A standard uncertainty due to run-to-run repeatability of 1.57 Pa and a Type B standard uncertainty associated with instrumentation of 2.89 Pa, resulting in a combined standard uncertainty of 3.29 Pa and an expanded uncertainty of ± 6.58 Pa at approximately 95% confidence ($k = 2$).

2.4 Distortion Quantification

To quantify distortion at the fan face, conventional metrics such as DC_{60} are commonly used and have proven effective for under-the-wing engine installations:

$$DC_{60} = \frac{\overline{p}_{t,\mathrm{AIP}} - \overline{p}_{t,60^\circ,\ \mathrm{min}}}{\overline{q}_{\mathrm{AIP}}} \tag{3}$$

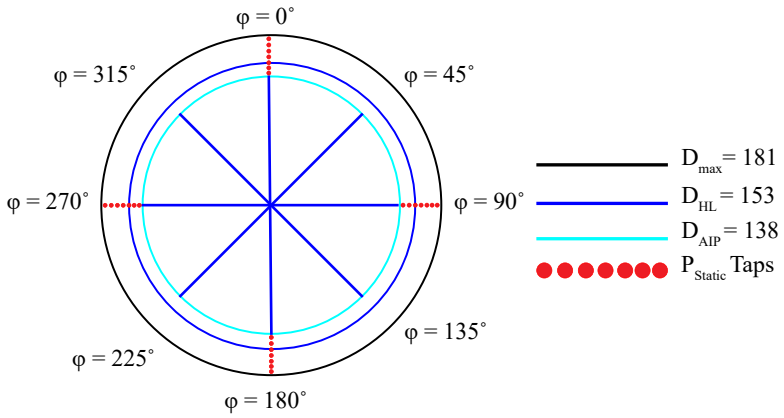
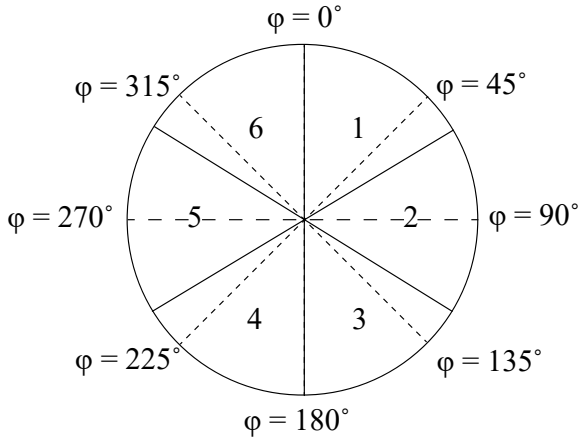
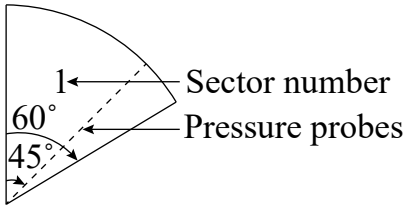


Figure 5 – Schematic of the rake locations at azimuthal intervals of 45° (φ), taps locations at azimuthal intervals of 90° (φ), and the corresponding diameters at various nacelle locations, including the Aerodynamic Interface Plane (AIP), highlight (HL), and maximum diameter (max). All diameters are given in millimetres (mm).

Equation 3 shows the definition of the DC_{60} parameter, where DC_{60} is the 60° total pressure distortion coefficient, $\overline{p}_{t,\text{AIP}}$ is the area-averaged total pressure at the aerodynamic interface plane (AIP), $\overline{p}_{t,60^\circ,\,\text{min}}$ is the minimum area-averaged total pressure evaluated over all six 60° circumferential sectors at the AIP, and $\overline{q}_{\text{AIP}}$ is the area-averaged dynamic pressure at the AIP.
Figure 6a shows a schematic of the AIP with rakes at $\varphi = 45^\circ$ intervals, indicated by dotted lines. Six 60° sectors are depicted by solid lines for the DC_{60} calculation. This is further illustrated in Figure 6b, where the first sector is isolated and annotated with its sector number and angular extent.



(a) A schematic of sector definitions of the AIP. The dotted lines signify the rake location, and the solid lines signify the boundaries between sectors.



(b) A detailed schematic of one sector

Figure 6 – Overview of sector definition for DC_{60}

The local pressure recovery contours presented in Section 3.2 for various mass flow ratios and angles of attack indicate that pressure-deficit regions can extend up to half of the AIP under certain flow conditions. As a result, the distortion pattern for this inlet spans multiple sixty-degree sectors. Therefore, alternative distortion descriptors that account for wider circumferential extent or full-face momentum deficits are required. Therefore, in addition to the DC_{60} parameter, a DC_{180} distortion metric is formulated to further characterize the circumferential total pressure distortion at the aerodynamic interface plane (AIP). The DC_{180} parameter is evaluated over 180° circumferential sectors, which are sequentially rotated in 45° increments starting from $\varphi = 0^\circ$.
This approach enables identification of the sector exhibiting the maximum distortion and provides additional insight into the spatial distribution of distortion beyond that captured by DC_{60}. The following

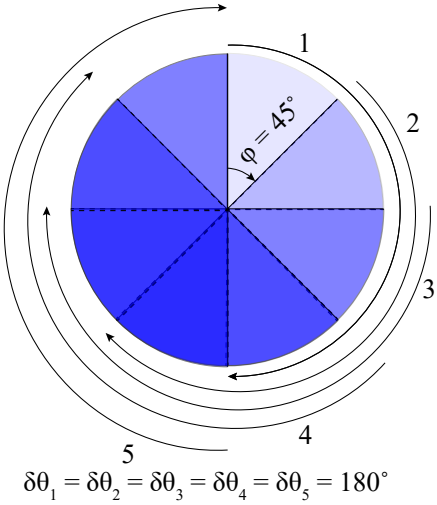


Figure 7 – A schematic of all sectors for DC_{180}. Each sector is $180°$, which is then rotated by $45°$.

defintion is used for DC_{180}:

$$\begin{aligned} DC_{180,i} &= \frac{\overline{p}_{t,\mathrm{AIP}} - \overline{p}_{t,\ \delta\varphi_i}}{\overline{q}_{\mathrm{AIP}}}, \\ \varphi_i &= (i-1)\times 45°, \qquad i = 1,\ldots,5 \end{aligned} \tag{4}$$

where $DC_{180,i}$ is the $180°$ total pressure distortion coefficient for the ith circumferential sector, $\overline{p}_{t,\ \delta\varphi_i}$ is the area-averaged total pressure evaluated over the corresponding $180°$ sector at the AIP, φ_i denotes the starting circumferential angle of the sector, and $\overline{q}_{\mathrm{AIP}}$ is the area-averaged dynamic pressure at the AIP.

Figure 7 shows the sector definitions used for the semi-circle-based distortion metric. In the right-hand of the schematic, the reference sector is highlighted and annotated with its angular range. The dotted lines indicate the $45°$ rotation increments used to shift the $180°$ sector around the AIP and identify the sector exhibiting the highest distortion.

3. Results

This section discusses the results of the experimental campaign. All experiments are performed at a wind-tunnel velocity of 25 m/s, which translates to $M_\infty = 0.073$ and $\mathrm{Re}_{\bar{c}} = 1.2\cdot 10^6$ and for various mass flow ratios (MFRs). The mass flow ratio is defined as:

$$\mathrm{MFR} = \frac{\dot{m}_{\mathrm{AIP}}}{\dot{m}_\infty} = \frac{\rho_\infty V_{\mathrm{AIP}} A_{\mathrm{AIP}}}{\rho_\infty V_\infty A_{\mathrm{AIP}}} \tag{5}$$

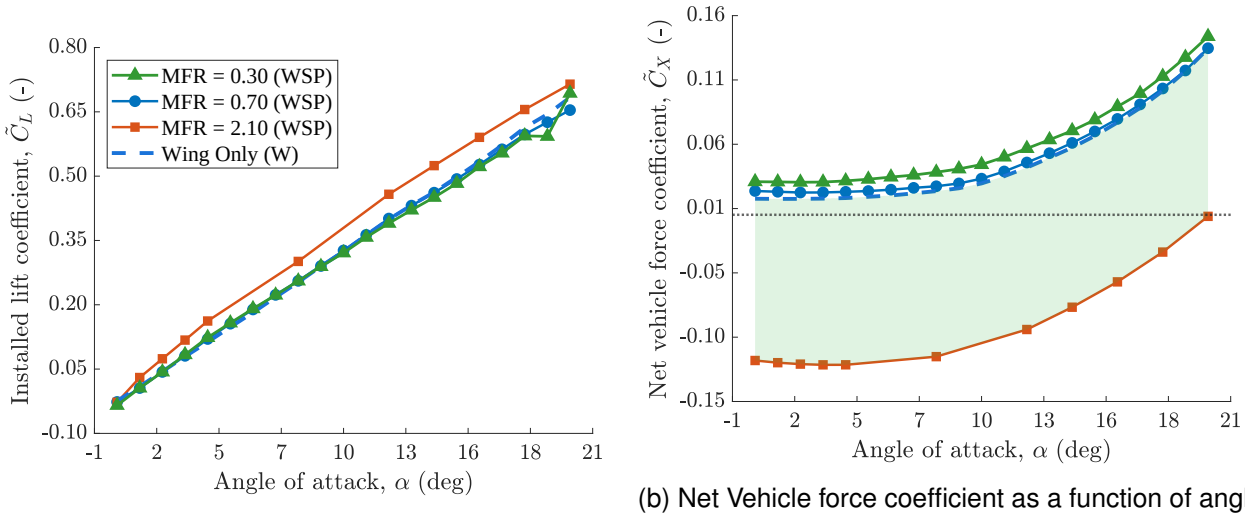
where $\dot{m}_{\mathrm{AIP}}$ denotes the mass flow rate through the Aerodynamic Interface Plane (AIP), and $\dot{m}_\infty$ is the freestream mass flow rate.

Section 3.1 discusses the aerodynamic forces generated by the engine installed on the highly-swept wing. Inlet pressure recovery for various mass flow ratios and angles of attack is presented in Section 3.2. Finally, inlet distortion results on the AIP are presented in Section 3.3.

3.1 Aerodynamic Forces

Figure 8 presents the installed lift and net vehicle force coefficients, $\tilde{C}_L$ and $\tilde{C}_X$, corresponding to the fully installed powered configuration (WSP), together with the wing-only reference (W), for three mass-flow ratios. The mass-flow ratios of 0.3, 0.7, and 2.1 correspond to windmilling, cruise, and take-off intake flow conditions, respectively.

For mass flow ratios of 0.3 and 0.7, the lift almost equals the lift of the isolated wing. The lift curve shifts upward with increasing mass flow ratio. At a mass-flow ratio of 2.1, the lift coefficient increases by approximately 0.03 with respect to the clean wing. The slope of the lift coefficient of the isolated wing remains nearly constant for all angles of attack. Figure 8b shows the net vehicle force coefficient $\tilde{C}_X$ as a function of angle of attack for the three MFRs. The region below the *wing-only* curve is



(a) Lift coefficient as a function of angle of attack

(b) Net Vehicle force coefficient as a function of angle of attack

Figure 8 – Installed lift coefficient and net vehicle axial-force coefficient together with the wing-only reference as a function of angle of attack for different mass-flow ratios at $Re_{\bar{c}} \approx 1.2 \times 10^6$ and $M_\infty = 0.07$

shaded light green to indicate conditions where the net thrust of the installed configuration exceeds the isolated-wing drag. Overall, $\tilde{C}_X$ increases with both α which is primarily caused by the increase in lift-induced drag. At a mass flow ratio of 0.3 (wind milling), the zero-lift drag coefficient increases by 35% with respect to the clean wing, although an unknown part of this is attributed to the addition of the support strut. The change in net vehicle force (thrust minus drag) with angle of attack is independent of the mass flow ratio. At MFR = 2.1, the installed net vehicle force remains higher than the wing-only case for all angles of attack. The change in the $\tilde{C}_X$ relative to the isolated wing remains largely independent of the angle of attack for all the MFRs. At a mass flow ratio of 2.1 and an angle of attack of four degrees, the net vehicle force is nine times higher than the drag of the clean wing. The magnitude of the reduction in net vehicle force coefficient decreases from approximately 1000% at $\alpha = 0°$ to 100% at $\alpha = 20°$, indicating a reduced relative thrust contribution with increasing angle of attack.

3.2 Inlet Pressure Recovery

Engine inlet performance is evaluated through the total pressure recovery at the AIP. The inlet pressure recovery is defined as $\mathrm{PR} = p_{t_{\mathrm{AIP}}}/p_{t_\infty}$, where $p_{t_{\mathrm{AIP}}}$ is the total pressure at the aerodynamic interface plane (AIP) and p_{t_∞} is the freestream total pressure.

Inlet pressure recovery as a function of angle of attack is shown in Figure 9 for three mass-flow ratios. Under windmilling conditions, the pressure recovery is highest at lower angles of attack (α) and decreases steeply beyond $\alpha = 10°$. After $\alpha = 10°$, the rate of decrease becomes more gradual. For the cruise condition (MFR = 0.7), the overall pressure recovery remains above 94% across the operational angles of attack ($2° < \alpha < 4°$). The steady reduction in pressure recovery is likely caused by the ingestion of the boundary layer, which tends to grow on the suction side with increasing angle of attack. For the takeoff condition (MFR = 2.10), the pressure recovery at $\alpha = 0°$ starts relatively low (91%). The converging streamtube towards the inlet is thought to ingest even more low-momentum air from the boundary layer. Interestingly, the reduction in pressure recovery with angle of attack is less compared to the other two mass flow ratios. At $\alpha = 12°$, the pressure recovery values for all cases coincide to approximately 78%.

For further analysis of the pressure recovery distribution over the AIP, a representative set of cases has been selected. The corresponding operating angles of attack are summarized in Table 2.

The selected cases are chosen based on the relevant operational ranges of angle of attack for each mass flow ratio. For the cruise condition (MFR = 0.7), lower angles of attack are considered, as these are representative for typical cruise operation. In contrast, a wider range of α values is examined for

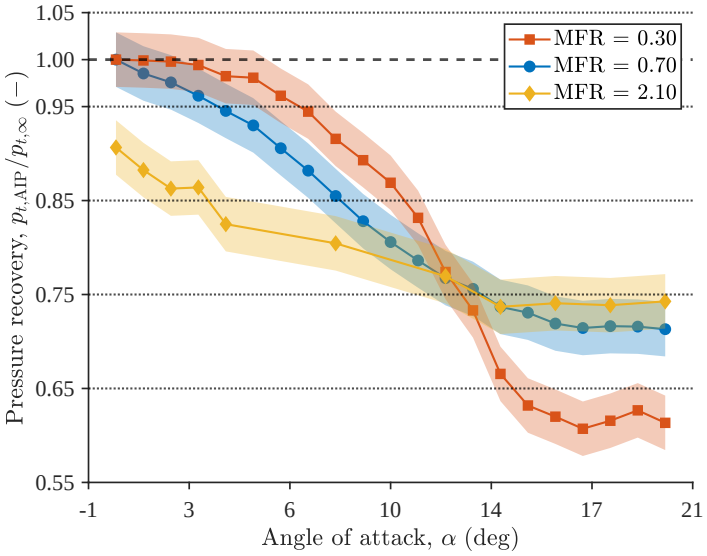


Figure 9 – Pressure Recovery as a function of angle of attack (α) for three mass flow ratios (MFRs). The transparent band around each line indicates the measurement error at $Re_{D_{HL}} \approx 2.1 \times 10^5$ and $M_\infty \approx 0.07$

Table 2 – Operating Conditions for Different Angles of Attack and Mass Flow Ratios

MFR	α **(deg)**	**Operating Cond.**
0.3	$0°, 4°, 8°, 16°$	OEI
0.7	$0°, 2°, 4°, 6°$	Cruise
2.1	$0°, 4°, 8°, 16°$	Take-Off, AEO

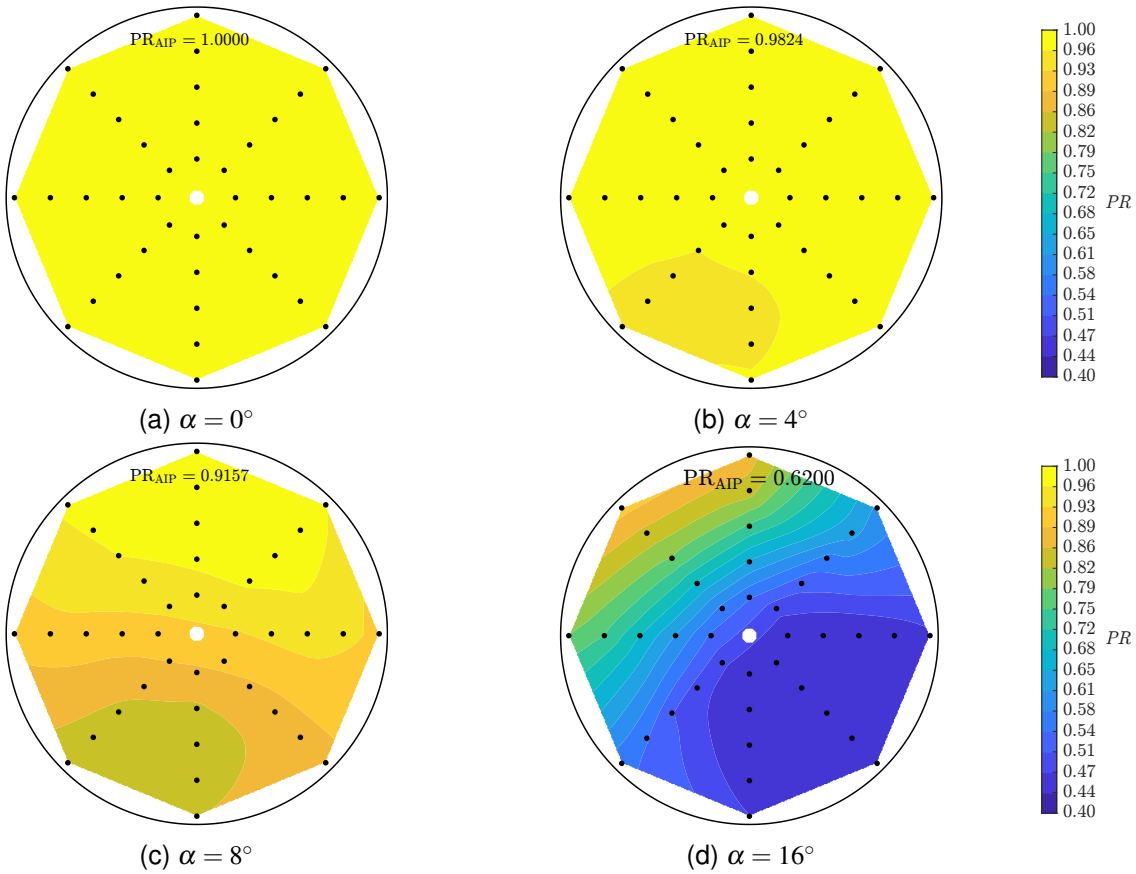
the take-off conditions with all engines operating (AEO) and one engine inoperative (OEI) to capture their broader operating envelopes. Figures 10, 11, and 12 present the local pressure recovery contours for the selected cases, providing further insight into the flow behavior under different operating conditions. In the following paragraphs, each figure is further discussed.

For the windmilling case (figure 10), the pressure recovery is close to one across the entire AIP for $\alpha \leq 4$, indicating that most of the wing's boundary layer passes below the intake lip. The local pressure recovery changes quite drastically at higher angles of attack, with local pressure recovery values being as low as 0.4, as shown in Figure 10d, at $\alpha = 16°$. The lowest pressure recovery value is found in the bottom right quadrant of the AIP, where the inlet is closest to the suction-surface of the wing (see Fig. 3b). This indicates that wake flow is ingested in the inlet.

Figure 11 shows the inlet total pressure recovery for the simulated cruise operating condition. The total pressure recovery decreases from 99% at $\alpha = 0°$ to 95% at $\alpha = 4°$. This 4% reduction can primarily be attributed to the increase in the adverse pressure gradient with angle of attack, which thickens the boundary layer. The local pressure recovery distribution indicates a deficit in total pressure in the lower portion of the AIP. In contrast, the upper two quadrants of the AIP exhibit unity pressure recovery at all angles of attack shown in Figure 11.

At the highest mass flow ratio of 2.1, corresponding to the takeoff condition, the total pressure recovery does not exceed 90% at any angle of attack. The local pressure recovery distribution at various angles of attack is shown in Figure 12. Notably, the local pressure recovery in the lower portion of the AIP is as low as 20% even at $\alpha = 0°$. At high angles of attack this reduction in local pressure recovery becomes less than 10% in some regions. This behavior is attributed to the ingestion of the wing boundary layer by the intake, as the fan's high suction draws in flow subjected to the wing's adverse pressure gradient. The resulting low-momentum air leads to a significant reduction in total pressure recovery at the AIP.

The region of reduced pressure recovery varies with the angle of attack, irrespective of the mass-flow ratio. At lower angles of attack, this region is centered around $\varphi = 180°$, while at higher angles of



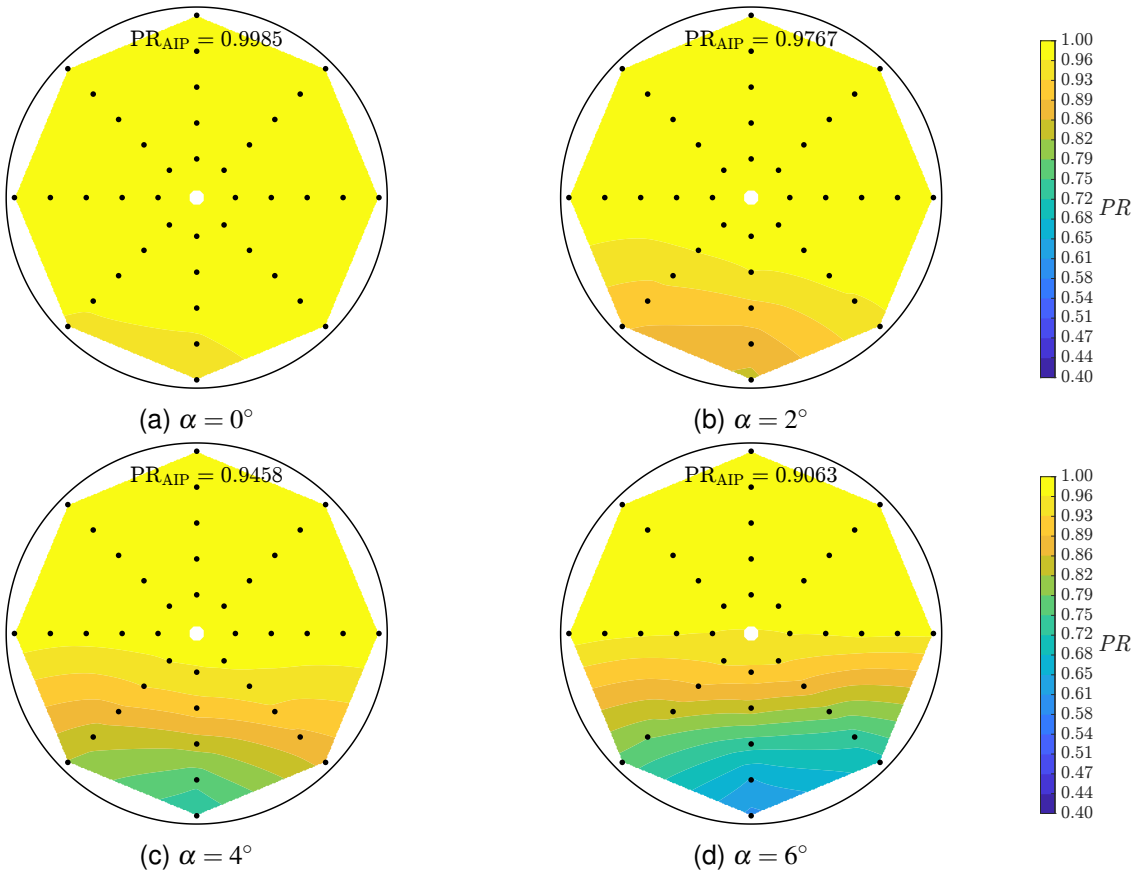
(a) $\alpha = 0°$ (b) $\alpha = 4°$

(c) $\alpha = 8°$ (d) $\alpha = 16°$

Figure 10 – Local pressure recovery contours at various angles of attack (α) for mass flow ratio (MFR) of 0.3. The total pressure recovery for each configuration has been annotated at the top of the contour plot. Black dots indicate the location of the total pressure probes on AIP.

attack it shifts to approximately $\varphi = 90°$. The reduction in pressure recovery with increasing angle of attack follows the same overall trend for all mass flow ratios, but is most pronounced at the highest mass flow ratio. At lower mass flow ratios, the region of decreased pressure recovery spans approximately $135° < \varphi < 225°$.

This behavior can be attributed to the engine installation location, which results in different local flow features, as shown in Figure 13. In this figure, location A is on the inboard side of the AIP, while location B is on the outboard side. The differing flow characteristics at locations A and B arise from the swept-wing flow field, which includes both chordwise and spanwise velocity components. With increasing angle of attack, trailing-edge vortices are generated, which then intensify, especially near the outboard wing region at location B. A part of the flow near the trailing edge enters from pressure to the suction side after $\alpha > 12°$ as shown by Viet [20]. This movement is promoted by the local pressure difference across the trailing edge and the strong three-dimensional boundary layer. When this flow enters the suction side boundary layer, which is already dominated by crossflow and an adverse pressure gradient, it introduces additional spanwise momentum and enhances three-dimensional mixing. As a result, the chordwise-to-spanwise velocity ratio decreases. This reduces the chordwise kinetic energy required to overcome the adverse pressure gradient, thereby reducing the boundary-layer deceleration efficiency. This leads to a decrease in the inlet pressure recovery. As the angle of attack increases, this migration occupies a larger area on the suction side. A similar migration in the outboard wing has been observed by van Luijk and Vos [21]. Since the trailing-edge flow is already subjected to an adverse pressure gradient, the combined effects of wing sweep, spanwise flow, trailing-edge vortices, and the migration of flow from the pressure side to the suction side cause the location of minimum local pressure recovery to move counterclockwise from approximately $\varphi = 225°$ toward $\varphi = 90°$.



(a) $\alpha = 0°$ (b) $\alpha = 2°$

(c) $\alpha = 4°$ (d) $\alpha = 6°$

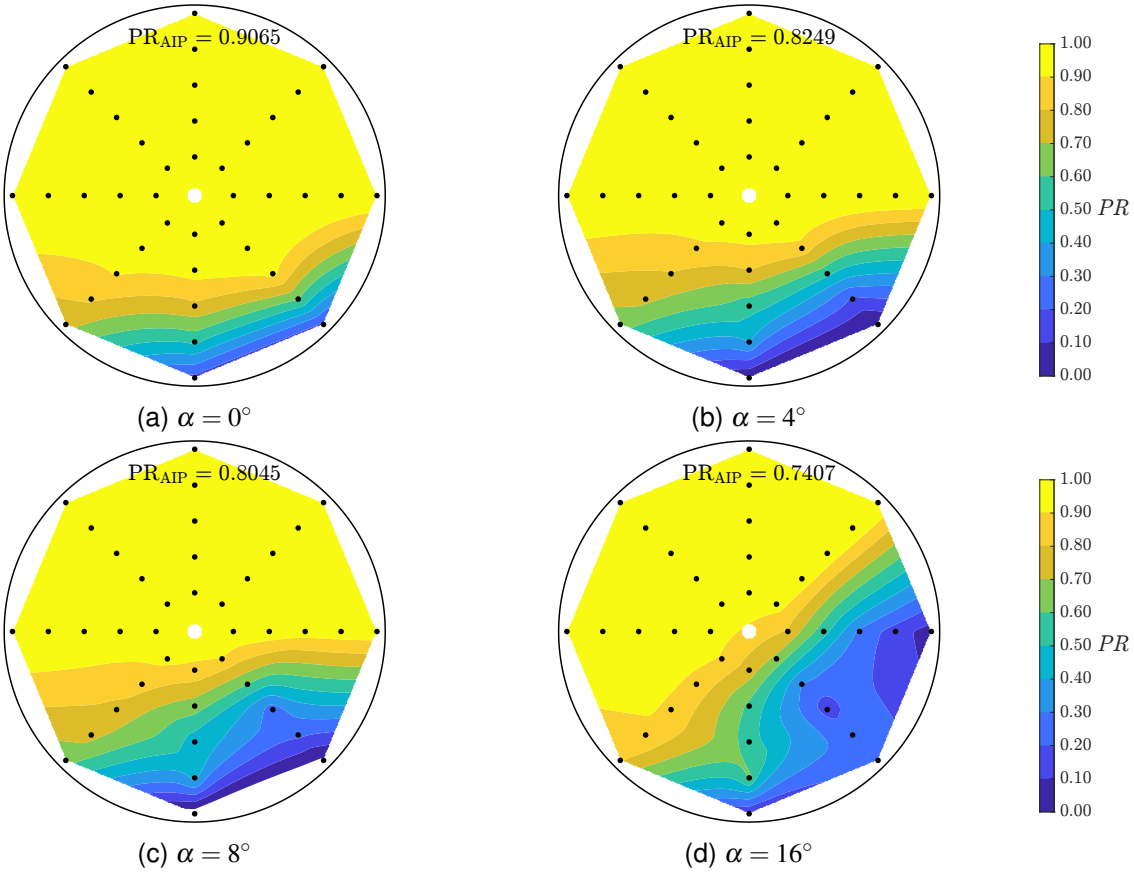
Figure 11 – Local pressure recovery contours at various angles of attack (α) for mass flow ratio (MFR) of 0.7. The total pressure recovery for each configuration has been annotated at the top of the contour plot. Black dots indicate the location of the total pressure probes on AIP.

3.3 Inlet Distortion

Apart from pressure recovery, inlet distortion plays an important role in over-the-wing engine installations, where the swept-wing flow interacts with the engine intake. While reduced inlet pressure recovery can be partially mitigated through improved fan design to achieve the required fan pressure ratio for a given thrust, flow distortion at the fan face results in circumferentially varying blade inflow angles, which can cause blade vibrations. Quantification of the distortion level at the AIP is therefore important. Following the definitions from Section 2., the distortion coefficients DC_{60} and DC_{180} are presented in the following paragraphs.

Figure 14 shows the DC_{60} for various angles of attack (α) and various mass flow ratios (MFR). For the windmilling intake condition of MFR = 0.3, the distortion is the least at all angles of attack, which could also be verified through Figure 10. At higher angles of attack, the distortion becomes highest as the minimum pressure recovery shifts towards $\varphi = 135°$ from $\varphi = 180°$. At the cruise condition of MFR = 0.7, the distortion is comparatively higher than at MFR = 0.3. For cruise conditions where the aircraft is operated at angles of attack less than $\alpha < 6°$, the values are less than 10%.For the take-off condition where the MFR = 2.1, the highest DC_{60} is around 40% at $\alpha = 8°$. The distortion is higher than 35% for all $\alpha \geq 4°$. In conjunction, the pressure recovery for $\alpha \geq 4°$ drops below 85%.

The increased inlet distortion associated with highly non-uniform inflow typical of boundary-layer-ingesting (BLI) configurations was investigated by [22] using RANS-derived fuselage boundary-layer profiles from clean-airframe CFD solutions. At cruise, the SAX40 blended-wing body with over-the-wing inlets ingests a boundary layer equivalent to 17% of aircraft drag, with parametric studies varying ingested boundary-layer thickness from 10% to 59% of inlet throat height. Over this range, the AIP total pressure recovery decreases from $PR = 0.96$ to $PR = 0.92$, while circumferential distortion increases from $DC_{60} = 0.25$ to $DC_{60} = 0.51$. For SAX40-representative ingestion levels (20–33%), the mass-averaged inlet pressure recovery is $PR \approx 0.95$ with DC_{60} in the range 0.32–0.42, depending on



(a) $\alpha = 0°$ (b) $\alpha = 4°$

(c) $\alpha = 8°$ (d) $\alpha = 16°$

Figure 12 – Local pressure recovery contours at various angles of attack (α) for mass flow ratio (MFR) of 2.1. The total pressure recovery for each configuration has been annotated at the top of the contour plot. Black dots indicate the location of the total pressure probes on AIP.

inlet duct geometry.

In contrast, in the present work, the inlet flow non-uniformity arises primarily from wing–nacelle aerodynamic interaction rather than direct boundary-layer ingestion, as a minimum clearance of approximately 13 mm is maintained between the nacelle and wing surface. Under cruise intake conditions with a freestream-to-AIP velocity ratio of approximately 0.7, the resulting distortion (DC_{60}) remains below 5%, with inlet total pressure recovery of approximately 95% at $\alpha = 4°$.

Figure 15 presents the worst-case DC_{180} values, computed using 4, as a function of angle of attack for all three mass flow ratios. As the angle of attack increases, the location of the worst distortion sector shifts from sector 3 to sector 2, as indicated by the different marker colors. This transition

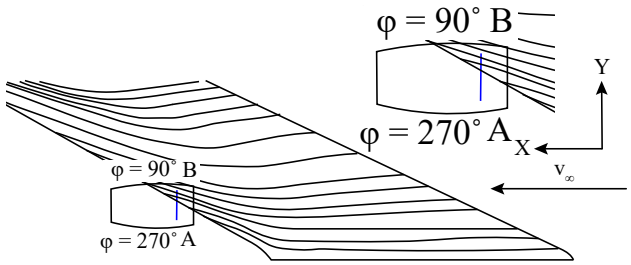


Figure 13 – A schematic of the envisioned flow field in the vicinity of the engine with a zoomed-in view near the nacelle location. The blue line indicates the two azimuthal rake locations at the aerodynamic interface plane (AIP). The surface stream traces are adapted from a cruise CFD simulation of a full-scale (Mach 0.85, Re $= 10^8$, $\alpha = 3°$) Flying V wing presented by Kumar and Vos [16].

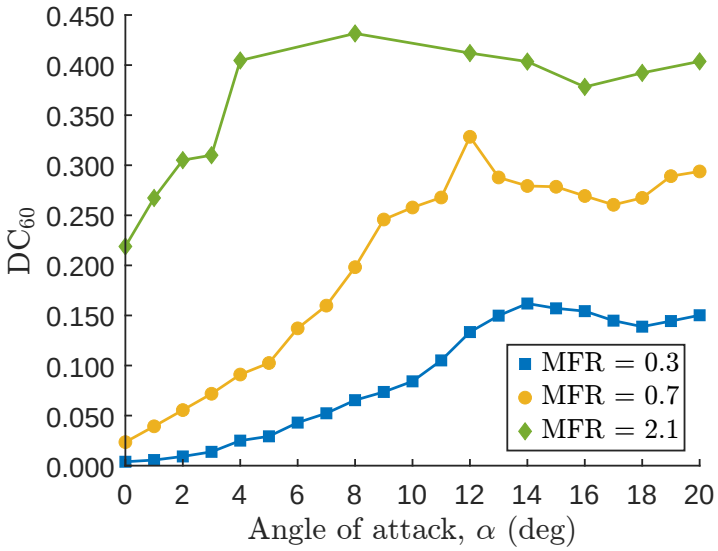


Figure 14 – Distortion Coefficient (DC_{60}), as a function of angles of attack for three mass flow ratios

occurs at $\alpha = 11°$ for MFR = 0.7 and 2.1, while for MFR = 0.3 it is delayed until $\alpha = 12°$.

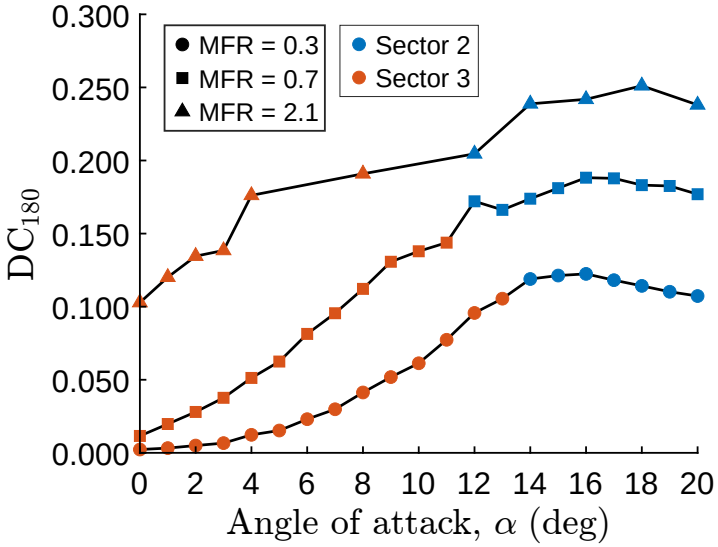


Figure 15 – Worst Distortion Coefficient (DC_{180}), as a function of angles of attack for three mass flow ratios

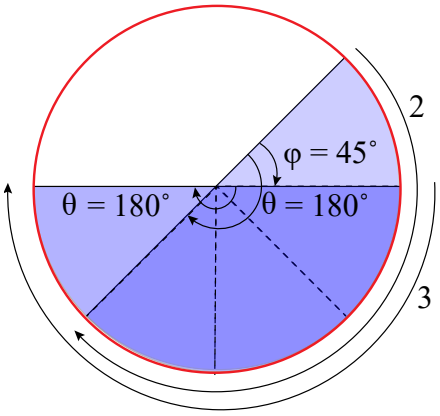


Figure 16 – A schematic of the second and third $180°$ sectors used for DC_{180}

For MFR = 0.3, the observed changes in trend are consistent across both distortion descriptors, DC_{60}

and DC_{180}. In contrast, for higher mass flow ratios, a similar change in trend is only observed at lower angles of attack ($\alpha < 9^\circ$). The worst-case DC_{180} values are consistently lower than the corresponding DC_{60} values. This behavior is expected, as DC_{180} averages over a larger angular interval, inherently reducing the influence of local total pressure deficits.
The shift in the worst distortion sector is further illustrated in the schematic shown in Figure 16, where both critical sectors are highlighted for clarity. These sector transitions correlate well with the local pressure recovery distributions shown in Figures 10, 11, and 12. Together, these results provide insight into the regions where inlet distortion becomes dominant, reflecting the combined effects of wing-induced flow, boundary layer development, and wake interaction.
Overall, the DC_{180} analysis reinforces the trends identified in the pressure recovery discussion in Section 3.2 and provides a comprehensive assessment of inlet flow distortion within the nacelle across the range of mass flow ratios considered.
The combined analysis of DC_{180}, DC_{60}, and the inlet pressure recovery demonstrates that inlet distortion within the nacelle is not only magnitude-dependent but also spatially reoriented with increasing angle of attack. The systematic shift in the worst distortion sector, together with its independence on mass flow ratio, indicates a predictable distortion pattern driven by upstream aerodynamic phenomena such as boundary layer thickening and cross flow. These findings establish a coherent link between local pressure recovery and circumferential distortion metrics, enabling a reliable assessment of inlet performance across the operating envelope.

4. Conclusion

Engine installation for the over-the-wing engine, a highly swept Flying V aircraft, has been investigated experimentally at 25 m/s in an open jet wind tunnel. Aerodynamic forces and local pressures at the aerodynamic interface plane (AIP) of the inlet are measured through force and pressure transducers. An electrically-driven ducted fan, as well as a perforated plate, are used to achieve three mass flow ratios: 0.3, 0.7, and 2.1, corresponding to windmilling, cruise, and takeoff conditions, respectively.
The lift curve shifts upward with increasing mass flow ratio, while its slope remains largely unchanged. At a mass-flow ratio of 2.1, the lift coefficient increases by approximately 0.03 with respect to the clean wing. At a mass flow ratio of 0.3 (wind milling), the zero-lift drag coefficient increases by 35% with respect to the clean wing, although an unknown part of this is attributed to the addition of the support strut. The change in net vehicle force (thrust minus drag) with angle of attack is independent of the mass flow ratio.
For a mass-flow ratio of 0.7 (cruise), the total pressure recovery is above 95% for angles of attack below 3 degrees. However, pressure recovery decreases rapidly with increasing angle of attack, reaching 0.75 at $\alpha = 14^\circ$. At a mass-flow ratio of 2.1, the pressure recovery is significantly lower with a maximum of 91% at a zero-degree angle of attack. However, the decrease in pressure recovery with angle of attack is less aggressive than for the cruise scenario, with a pressure recovery of 0.75 at $\alpha = 14^\circ$.
The location of the maximum total pressure loss is shown to migrate from the lower half of the AIP towards the outboard side of the AIP as the angle of attack increases. With increasing mass-flow ratio, more wake flow from the wing is ingested, reducing average pressure recovery and leading to a large area with local pressure recovery below 40% at angles of attack of 8 degrees and higher. This results in high distortion levels with distortion coefficients DC_{60} and DC_{180} reaching as 40% and 25%, respectively, for a mass-flow ratio of 2.1 and angles of attack beyond 12 degrees.
To further understand engine inlet behaviour and aero-propulsive interactions, a detailed analysis of the nacelle surface pressure distribution is required to characterise the installed inlet flow field. Multi-hole probe measurements at the aerodynamic interface plane (AIP) is recommended, as the intake flow is expected to be highly nonuniform. The observed reduction in local pressure recovery should be investigated using time-resolved measurements to quantify dynamic distortion.

Acknowledgements

The authors would like to acknowledge Mr. Malcom Brown, Ms. Nikki van Luijk, Mr. Burhan Saify, Mr. Aaron Sequeira, Mr. Ardya Inderawan, Mr. Brian Dsouza, Ms. Debdutta Chatterjee, Mr. Buğrahan Öztürk, Dr. Jatinder Goyal, Mr. Vaibhav Mysore Natesh, and Dr. Kostas Moularas for helping during

the experimental campaign. The authors would also like to thank Mr. Stefan Bernardy for helping with the data acquisition system software for pressure scanners. The authors would also like to thank the wind tunnel facility manager, Henk-Jan-Seimer, and the lab technicians, Floris Blok and Dennis Bruikman, for their assistance with the measurement instruments and the wind tunnel. The authors would also like to acknowledge Mr. Ed Roessen, Mr. Peter den Dulk, Mr. Rob van der List, and Mr. Frank Schilder for manufacturing the nacelle test article.

5. Copyright Statement

The authors confirm that they, and/or their company or organization, hold copyright on all of the original material included in this paper. The authors also confirm that they have obtained permission, from the copyright holder of any third party material included in this paper, to publish it as part of their paper. The authors confirm that they give permission, or have obtained permission from the copyright holder of this paper, for the publication and distribution of this paper as part of the ICAS proceedings or as individual off-prints from the proceedings.

References

[1] International Energy Agency. World energy outlook 2023. Technical report, IEA, Paris, 2023.

[2] J. Benad. The flying v a new aircraft configuration for commercial passenger transport. In *Proceedings of Deutscher Luft- und Raumfahrtkongress*, Rostock, 22-24 September 2015.

[3] A. Marques Cavaleiro Machado Jorge. Quantifying wind tunnel effects on the flying v. Master thesis, TU Delft, Aerospace Engineering, 2023. Graduation committee members: N. L. M. van Luijk and F. Oliviero.

[4] A. R. García. Aerodynamic model identification of the flying v using wind tunnel data. Master thesis, TU Delft, Aerospace Engineering, 2019.

[5] A. R. García, M. Brown, D. Atherstone, N. v. Arnhem, and R. Vos. Aerodynamic model identification of the flying v from sub-scale flight test data. In *AIAA SCITECH 2022 Forum*.

[6] R. Torelli, O. Stroosma, Roelof Vos, and Max Mulder. Piloted simulator evaluation of low-speed handling qualities of the flying-v. In *AIAA SciTech Forum 2023*. American Institute of Aeronautics and Astronautics, 2023.

[7] G. Vugts, O. Stroosma, Roelof Vos, and Max Mulder. Simulator evaluation of flightpath-oriented control allocation for the flying-v. In *AIAA SciTech Forum 2023*. American Institute of Aeronautics and Astronautics, 2023.

[8] S. Joosten, O. Stroosma, R. Vos, and M. Mulder. Simulator assessment of the lateral-directional handling qualities of the flying-v. In *AIAA SCITECH 2023 Forum*, 2023. Final published version available via TU Delft Repository: https://resolver.tudelft.nl/uuid:efa4f555-d392-4438-8c61-43b2d211cf08.

[9] W. Oosterom and R. Vos. Conceptual design of a flying-v aircraft family. *AIAA AVIATION 2022 Forum*, 2022.

[10] J. Stougie, T. Pollack, and E. V. Kampen. Incremental nonlinear dynamic inversion control with flight envelope protection for the flying-v. In *AIAA SCITECH 2024 Forum*, pages AIAA 2024–2565, Orlando, FL, January 2024. Session: Nonlinear Dynamic Inversion Control.

[11] M. A. Saez Ortuño. Climate impact of hydrogen aviation: Research on the variations of surface temperature change caused by hydrogen and kerosene combustion aircraft. Master thesis, TU Delft, Aerospace Engineering, 2022.

[12] M. J. D. Reekers. Climate effects of the flying v. Master thesis, TU Delft, Aerospace Engineering, 2021.

[13] Y. Laar, D. Atherstone, J. Benad, and R. Vos. Aerodynamic design of a flying v aircraft in transonic conditions. *AIAA SCITECH 2024 Forum*, 2024.

[14] B. R. Pascual and R. Vos. The effect of engine location on the aerodynamic efficiency of a flying-v aircraft. *AIAA Scitech 2020 Forum*, 2020.

[15] S. v. Empelen and R. Vos. Effect of engine integration on a 4.6 *AIAA Scitech 2021 Forum*, 2021.

[16] A. Kumar, S. Asaro, and R. Vos. Aerodynamic analysis of the flying v subsonic transport to enable engine integration. *AIAA SCITECH 2025 Forum*, 2025.

[17] S. Asaro and R. Vos. Synthesis of the aerodynamic model of a flying wing aircraft. In *AIAA SCITECH 2025 Forum*, 2025.

[18] M. B. Rivers. Nasa common research model: A history and future plans. *AIAA Aviation 2019 Forum*, 2019.

[19] R. A. Van den Braembussche, T. Arts, M. Carbonaro, J. M. Charbonnier, G. Degrez, D. Olivari, and M. L.

Riethmuller. Measurement techniques in fluid dynamics: An introduction. Technical report, Von Karman Institute for Fluid Dynamics, 1994.

[20] Rob Viet. Analysis of the flight characteristics of a highly swept cranked flying wing by means of an experimental test. Master's thesis, Delft University of Technology, 2019.

[21] N. V. Luijk and R. Vos. Experimental investigation of vortex flow over a flying v subsonic transport. In *AIAA SCITECH 2025 Forum*, 2025.

[22] A. Plas, D. Crichton, M. Sargeant, T. P. Hynes, E. M. Greitzer, C. A. Hall, and V. Madani. Performance of a boundary layer ingesting (bli) propulsion system. *45th AIAA Aerospace Sciences Meeting and Exhibit*, 2012.